Article

Exceptionally high proton conductivity in Eu$_2$O$_3$ by proton-coupled electron transfer mechanism

$$H_2 + 2O_o^x \rightarrow 2OH_o^{\cdot} + 2e'$$
(1)

$$H_2O_{(g)} + O_o^x + V_o^{\cdot\cdot} \rightarrow 2OH_o^{\cdot}$$
(2)

Eu^{3+}
Eu^{2+}

- ⬤ Crystal lattice oxgyn
- ⬤ Water gas molecules
- ⬤ Oxygen vacancy
- • H$^+$

Shuo Wan, M. A. K. Yousaf Shah, Hao Wang, Peter D. Lund, Bin Zhu

zhu-bin@seu.edu.cn

Highlights

High proton conductivity, 0.1 S/cm at 500°C

The electrochemical proton injection process accompanied with relaxation times analysis (DRT)

Proton-coupled electron transfer (PCET) mechanism discovered in Eu$_2$O$_3$

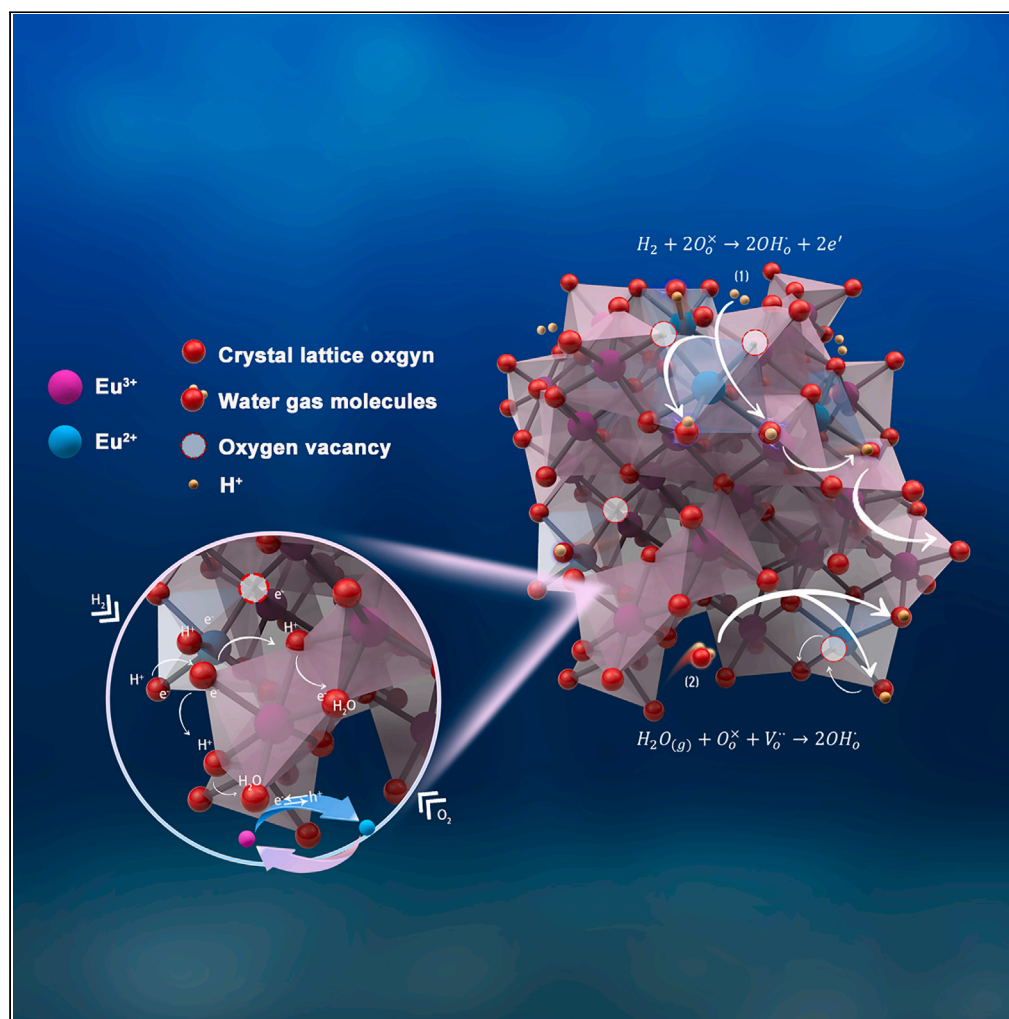PCET via a redox cation couple and the oxygen vacancy mechanism

Article

Exceptionally high proton conductivity in Eu$_2$O$_3$ by proton-coupled electron transfer mechanism

Shuo Wan,[1] M. A. K. Yousaf Shah,[1] Hao Wang,[1] Peter D. Lund,[1,2] and Bin Zhu[1,3,*]

SUMMARY

Proton conductors are typically developed by doping to introduce structural defects such as oxygen vacancies to facilitate ionic transport through structural bulk conduction mechanism. In this study, we present a novel electrochemical proton injection method via an *in situ* fuel cell process, demonstrating proton conduction in europium oxide (Eu$_2$O$_3$) through a surficial conduction mechanism for the first time. By tuning Eu$_2$O$_3$ into a protonated form, H-Eu$_2$O$_3$, we achieved an exceptionally high proton conductivity of 0.16 S cm^{-1}. Distribution of relaxation time (DRT) analysis was employed to investigate the proton transport behavior and reveal the significant contribution of surface proton transport to the overall conductivity of Eu$_2$O$_3$. Remarkably, H-Eu$_2$O$_3$ exhibited a low activation energy for ionic transport, comparable to the best ceramic electrolytes available. The proton-coupled electron transfer (PCET) mechanism describes this novel surficial proton conduction mechanism. These findings provide new possibilities for developing advanced proton conductors with improved performance.

INTRODUCTION

Proton ceramic fuel cells (PCFCs) have become a focus in solid oxide fuel cell (SOFC) research and development. BaCeO$_3$- and BaZrO$_3$-based perovskite oxides, first discovered by Iwahra et al. four decades ago,[1,2] have played a pivotal role in advancing the quest for viable PCFC materials. These perovskite oxides hold tremendous promise for PCFC applications due to their unique ability to operate at lower temperatures, setting them apart from traditional SOFCs that utilize fluorite-yttrium stabilized zirconia (YSZ) electrolytes. This distinctive characteristic opens up new opportunities for practical and widespread applications,[3] and has garnered significant interest in the field.

However, one of the primary challenges in PCFC development lies in the limited proton conductivity of existing BaZrO$_3$- and BaCeO$_3$-based materials at lower temperatures, typically ranging from 10^{-3} to 10^{-2} S/cm below 600°C. To achieve satisfactory fuel cell performance, a proton conductivity of around 0.1 S/cm is desired. This limitation has spurred intensive research efforts to identify and develop alternative materials that exhibit enhanced proton conductivity at these lower operating temperatures. Overcoming this barrier is urgent to realize the full potential of PCFCs as highly efficient and environmentally friendly energy conversion technologies.

Lowering the operating temperature to the range of 300°C–600°C is an emerging tendency for low-temperature SOFCs/PCFCs that highly demand alternative materials capable of transporting H$^+$ or O^{2-} or both. This shift toward lower operating temperatures offers several advantages, such as enabling the use of cheaper interconnects and sealing materials, prolonging the lifespan of fuel cells, allowing rapid start-up and shut-down, and expanding their application fields.[4]

In this context, there is a growing interest in exploring novel materials with enhanced proton conductivity or oxygen ion transport properties at lower temperatures. Such materials would pave the way for efficient and cost-effective low-temperature SOFCs and PCFCs, making them more accessible for widespread implementation in commercialization. As research progresses in this area, the realization of high-performance, low-temperature ceramic fuel cells (CFCs) become increasingly promising, unlocking new possibilities by alternative material solutions.

Regarding this concern, recent research in low-temperature CFCs has been focused on exploring various semiconductor membrane materials with enhanced proton or oxygen ion transport properties. Some of the key materials under investigation, such as SrTiO$_3$,[5] CeO$_2$,[6] TiO$_2$,[7] and various other metal oxide semiconductors.[8] Additionally, heterostructures composed of semiconductor-ionic composite systems have been investigated with some typical examples: CeO$_2$/CeO$_{2-\delta}$,[6] Ba$_{0.5}$Sr$_{0.5}$Co$_{0.1}$Fe$_{0.7}$Zr$_{0.1}$Y$_{0.1}$O$_{3-\delta}$-Ca$_{0.04}$Ce$_{0.80}$Sm$_{0.16}$O$_{2-\delta}$(BSCFZY–SCDC),[9] ZnO/MgZnO,[10] and BaCe$_{0.4}$Zr$_{0.4}$Y$_{0.1}$Yb$_{0.1}$O$_3$-Sm$_{0.2}$Ce$_{0.8}$O$_2$ (BCZYYb-SDC).[11] In this study, we focus on rare earth oxide (REO) materials, specifically the ultra-wideband gap (UWBG) n-type semiconductor europium oxide (Eu$_2$O$_3$). It exhibits intriguing optical, electrical, and structural properties, such as being an insulator,[12] low-voltage cathodoluminescent devices,[13,14] biomedical sensors,[15] catalysts,[16] and optoelectronic

[1]Jiangsu Provincial Key Laboratory of Solar Energy Science and Technology/ Energy Storage Joint Research Center, School of Energy & Environment, Southeast University, Nanjing 210096, China
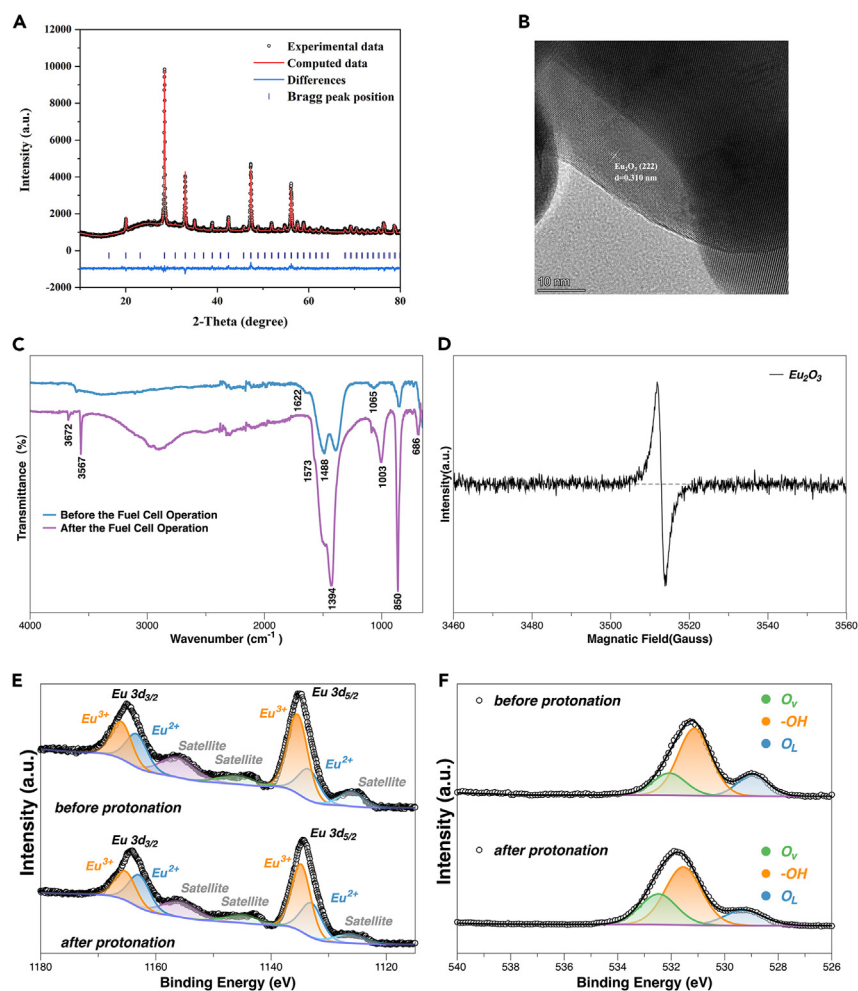[2]School of Science, Aalto University, P.O. Box 15100, 00076 Aalto, Espoo, Finland
[3]Lead contact
*Correspondence: zhu-bin@seu.edu.cn
https://doi.org/10.1016/j.isci.2023.108612

Figure 1. Characterization of the Eu$_2$O$_3$ electrolyte

(A and B) Diffraction patterns at 25°C (A), with representation of the related high-resolution TEM (B) of the corresponding main [222] facet. θ is the diffraction angle.

(C) The Fourier transform infrared spectra of the sample show two sharp peaks at 3567 cm^{-1} and 666.0 cm^{-1} are attributed to the O–H stretching and bending vibration.

(D) The electron paramagnetic resonance spectrum exhibits a strong signal at g = 2.003 due to unpaired electrons associated with the oxygen vacancy defects.

(E and F) The X-ray photoelectron spectra of the Eu 3d (E) and O 1s (F) show the content of oxygen vacancies and Eu (II) are both increased after the fuel cell operation.

devices.[17] However, its ionic conducting properties and its potential as a primary dopant, unlike samarium or lanthanum with trivalence used as dopant receptors,[18,19] have not yet been studied for adjusting the electrical and electrochemical characteristics of CFC electrolytes.

Surface and interface qualities have been identified as crucial factors in achieving superior ionic conduction and excellent fuel cell performance in semiconductors and semiconductor-ionic heterostructure materials.[6,9,11,18] While the inherent structure of Eu$_2$O$_3$ does not inherently support efficient ionic conduction or serve as a dopant for developing novel electrolytes, this study explores, for the first time, proton conduction in Eu$_2$O$_3$ through a surface conduction mechanism. We achieved this by *in situ* fuel cell electrochemically injecting protons into Eu$_2$O$_3$, which was tuned as a protonic electrolyte. Remarkable changes in its electrical properties were observed under stabilized operating conditions. A proton conductivity of 0.16 S cm^{-1} at 520°C was achieved, which is exceptionally high for proton conductor ceramic materials. The proton conduction was verified through isotopic, proton filter, distribution of relaxation time (DRT), and hydrogen partial pressure experiments.

RESULTS AND DISCUSSION

To characterize the structure of the commercial material, Rietveld refinement of the powder X-ray diffraction (XRD) data was conducted (Figure 1A). All the peaks in the XRD pattern can be well indexed by cubic phase (Ia-3) with parameters close to those for Eu$_2$O$_3$ (PDF#86–2476),[20]
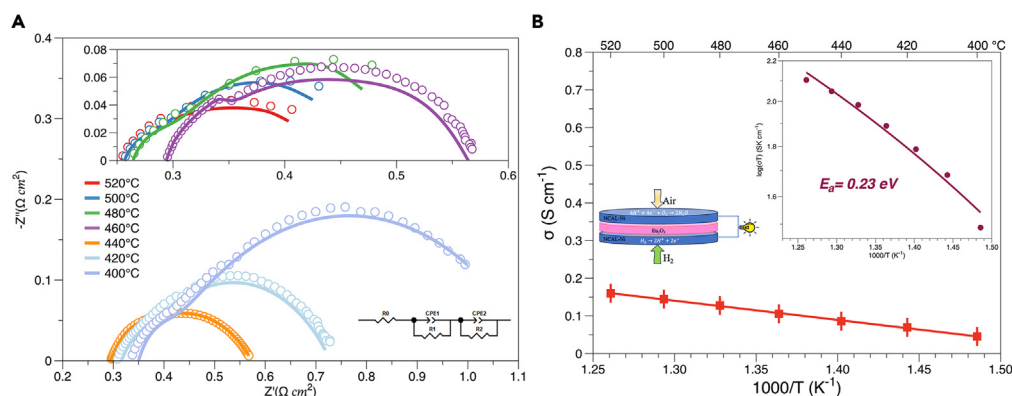
Figure 2. Electrochemical performance of the Eu2O3 electrolyte

(A) The impedance spectra were effectuated under the conditions of H_2/air from 400°C to 520°C, showing grain boundary resistance increases when the temperature drops.

(B) The corresponding Arrhenius plots obtained from the ohmic polarization region show an exceptionally high proton conductivity of 0.16 S cm^{-1} at 520°C.

no additional diffraction peaks are found, which indicates a pure crystalline phase of the Eu_2O_3 nanoparticles. Peaks at 28.48°, 33.00°, 47.34° and 56.14° correspond to (222), (400), (440), and (622) crystal planes, respectively. The final refinement was stable with low R-factors (Table S1). The high-resolution transmission electron microscopy (HRTEM) image in Figure 1B displays the clear lattice fringes for the sample. It shows that the interplanar spacing of the crystalline is 0.310 nm, identical to the main (222) facet distance of the cubic Eu_2O_3 phase.

Fourier transform infrared (FTIR) spectra of the sample deliver crucial hydrogen bonding information after fuel cell operation (Figure 1C). The appearance of new peaks in the protonated H-Eu_2O_3 spectrum suggests the formation of new chemical bonds or structural changes in the material due to protonation. It can be seen clearly that two sharp peaks at 3,567 cm^{-1} and 3,672 cm^{-1} could be attributed to the structural O–H stretching vibrations[21,22] confirming the presence of the protonated species in the sample. A very broad band in a range from 2,700 cm^{-1} to 3,450 cm^{-1} suggests the presence of adsorbed water molecules on hydroxyl groups on the surface,[22–24] which is common in metal oxide with high surface area and high reactivity, showing a significant impact on its chemical and physical properties, such as its catalytic activity and surface charge. Another peak at 1,622 cm^{-1} or 1,573 cm^{-1} is assigned to the bending mode of H-OH adsorbed on surface.[24] And two strong peaks at 1,488 and 1,394 cm^{-1} are possibly due to the oxygen ions' stretching vibrations and the bending mode of O-H.[25,26] When protons are injected into the lattice and interact with oxygen ions, the vibrational frequency of oxygen ions changes, making the double peaks degenerate and shift to a single peak with a shoulder. And the bands at around 686 cm^{-1} are assigned to the bend vibration of Eu-*O*-H.[27] Other signals at 1,065 cm^{-1}, 1,003 cm^{-1}, and 857 cm^{-1} may be assigned to C-O, C-H, and CH_2, due to Eu2O3 easily absorbing carbon dioxide from the environment.

The oxygen vacancies and lattice oxygen on the surface are potent proton acceptors,[28] contributing to the formation of forming these strong hydrogen bonds in oxides. These coupled O-Hs are produced in the cell's operating environment at 520°C, so the proton path and diffusion are testified. The electron paramagnetic resonance (EPR) experiment was conducted on the dry powder Eu_2O_3 to get more information about oxygen vacancy defect distribution.[29] The sample exhibits a stronger paramagnetic resonance signal at g = 2.003 due to unpaired electrons associated with the oxygen vacancy defects, i.e., the Eu_2O_3 sample has a sizable fraction of oxygen vacancy defects (Figure 1D).

Moreover, X-ray photoelectron spectroscopy (XPS) was used to examine the chemical and oxidation states along with surface properties of Eu_2O_3—calibration of the results followed by binding energy (BE) referencing method.[30] The Eu (3d) spectrum (Figure 1E) is divided into two BE groups, d$_{5/2}$ and d$_{3/2}$, due to the spin-orbit coupling effect of the Eu 3d core level.[31] In the spectra, two significant peaks near 1,135 eV and 1,165 eV correspond to Eu (III), and two weaker peaks close to 1,133 eV and 1,163 eV are denoted by Eu (II). A fraction of Eu (II) originates from the surface layer due to a "surface-valence-transition" phenomenon observed in Eu2O3 before.[32] The coexistence of the Eu (II) and Eu (III) states may induce oxygen defects and enhance electrochemical processes' electron transport and kinetics.[32] O 1s peaks (Figure 1F) can be split into three types of peaks located nearby at 529 eV, 531 eV, and 532 eV, respectively, which refers to crystal lattice oxygen, oxygen species integrated on the surface, and compensation of deficiencies, i.e., oxygen vacancies in the oxides.[33] After the fuel cell operation, the peak area of oxygen vacancy, O_v, is enhanced from 20.17% to 29.19%, which can support proton pathways. The Eu (II)'s presence increased from 28.88% to 35.9% (Table S2).

The fuel cell using the Eu_2O_3 as the electrolyte exhibits an outstanding maximum power density of 660.89 mW cm^{-2} at 520°C and open-circuit voltages (OCVs) from 400°C to 520°C are all exceeding 1V indicating a negligible electronic leakage (Figure S3). Figure S2 shows the cross-section scanning electron microscope (SEM) images of Eu_2O_3, including an amplified view for matching between the electrode and electrolytes as well. Electrochemical impedance spectroscopy (EIS) spectra were obtained under the conditions of H_2/air (120 mL/min) from 400°C to 520°C after the voltage has stabilized as shown in Figure 2A. According to the EIS fitting curves and Table S3, the sample conductivities can be calculated. Figure 2B displays Arrhenius plots, i.e., temperature dependence for conductivities (σ) from which the activation

energy for ion transport is obtained to be 0.23 eV.[34–37] What's more, we have compared the astonishing ionic conductivity of Eu_2O_3 with that of the electrolyte commonly used in SOFCs, as shown in Figure S4.

Several experimental methods were applied to study the proton transportation in Eu_2O_3. Firstly, we carried out isotope measurements. The Eu_2O_3 sample exhibits a clear conducting difference in the D_2 and H_2 atmospheres (Figure S5C). The big difference between ^1H and D indicates an isotope effect, i.e., proton conduction in Eu_2O_3. When H^+ and D^+ are incorporated in Eu_2O_3 to form hydro/deuteroxyl groups (OH^- or OD^-), deuterons migrate at a lower rate than protons and hydro/deuteroxyl groups to cause such a big difference in their conductivities (Table S4).

$$H_2 + 2O_o^{\times} \rightarrow 2OH_o^{\cdot} + 2e' \tag{Equation 1}$$

$$D_2 + 2O_o^{\times} \rightarrow 2OD_o^{\cdot} + 2e' \tag{Equation 2}$$

Secondly, the well-known proton conductor BZCY was added at both sides as a proton filter layer to verify proton transportation.[38] The performance of cells with a configuration of NCAL/BZCY/Eu_2O_3/BZCY/NCAL is 582.05 mW cm^{-2}, which is 86.05% of that without proton filter (Figure S5A). This drop in the power output can be ascribed to the following. (1) The BZCY layers' resistances. (2) Two additional interfaces between the Eu_2O_3-sample and BZCY layers leading to additional resistances. These can be further analyzed from EIS that the ohmic resistances increased from 0.248 Ω cm^2 to 0.291 Ω cm^2, and the grain boundary resistances increased from 0.025 Ω cm^2 to 0.034 Ω cm^2, respectively, for the cells without and with the BZCY layers (Figure S5B). (3) Two interfaces between the NCAL electrode and BZCY layers result in more significant polarization resistance losses, increasing from 0.166 Ω cm^2 to 0.176 Ω cm^2, respectively, for the cells without and with the BZCY layers (Table S5). These disparities indicate that extra BZCY layers can result in a 14.95% power loss. Therefore, it can be inferred that proton transport in the Eu_2O_3 electrolyte is the primary contributor to ionic transport and fuel cell power output.

Further key evidence is provided by the equivalent circuit scheme (ECS) method with the DRT analysis[39–42] during the electrochemical proton injection process via a Eu_2O_3 electrolyte fuel cell at a fixed temperature of 520°C. Although this method utilizes a similar setup to a fuel cell device, the purpose and measuring procedures are distinct with a controlled small hydrogen flow for the device activation and measure *in situ* process for the conducting properties. This methodology investigates the conducting transition from intrinsic oxygen-ion conduction to the preferential injection of protons positioned at the surface of the particles, resulting in a surficial proton transport. We employed a low flow rate of H_2 at 30 mL/min to activate the device and air at the same flow rate, too, while EIS measurements were taken every 10 min from air/air shifted to H_2/air (FC) environments. The DRT analysis can identify the polarization processes with a high resolution and discern the electrochemical processes that overlap in the EIS curve.[43] The peaks in the DRT profile refer to their sub-processes, and the area under the peak reflects the simulated resistance corresponding to that sub-process.[44] In other words, the smaller the peak area, the less obstruction to the process on going. Therefore, the proportions of each sub-process in the total resistance are obtained by calculating the area ratio of the peak in DRT curves (Figure S6). In specific, the conductivity in a pure air atmosphere is 2.01 × 10^{-5} S/cm, while in the first 50 min (Figure 3C), the conductivity calculated by EIS data (Table S6) increases ceaselessly to a stable plateau within 30 min after hydrogen introduction and proton injected into Eu_2O_3. Then the change rate gradually slows down until the conductivity reaches 0.10 S/cm. The attained conductivity results have precisely proved that an electrochemical proton injection occurs in Eu_2O_3. Since the sample is from the air, no proton concentration exists initially. Subsequently, one side of the air was replaced by hydrogen. The cell resistance reduced dramatically over time, resulting in a rather high proton concentration incorporation into the sample, so the Eu_2O_3 was tuned to exhibit a high and stable proton conductivity.

More detailed DRT analysis as illustrated in Figure 3A, oxygen is predicted to dominate the reduction reaction catalyzed by electrodes in air, corresponding to the P_4' peak accounting for 86.2% of the entire process.[43,45] Similarly, the P_5' and P_6' peaks in this low-frequency region are associated with oxygen adsorption, dissociation, and gas diffusion processes, respectively.[45] And in the first 60 min after a small flow of hydrogen was introduced in the cell, the impedance spectra revealed six discernible peaks in the electrochemical reaction process. P_1 peaks correspond to the proton interfacial or grain boundary conduction, including diffusing to the electrolyte surface. P_2 peaks represent the hydrogen adsorption and dissociation, proton formation, and lattice incorporation.[46–48] P_3 peaks are situated at an intermediate frequency region, reflecting oxygen incorporation into the lattice and bulk diffusion of protons to the triple-phase boundary (TPB), respectively.[43,45] Based on the oxygen reduction reaction (ORR) catalyzed in the air side, the ORR effect will be further superimposed with the introduction of hydrogen, which indicates P_4 peaks to be related to oxygen reduction and oxygen surface diffusion to TPB.[43,45] Moreover, based on the location analysis of the aforementioned peaks in air/air and H_2/air conditions, P_5 and P_6 peaks that recurred from the thirtieth minute onward suggest oxygen adsorption, dissociation, and water formation processes, respectively, as well as gas diffusion and water evaporation processes[43,45] (Table S7).

Considering all peak areas have decreased significantly after the hydrogen introduced into the system, to be more specific, comparing the P_4 and P_4' peak areas of the ORR process, we can see that the corresponding resistance under air is 2,490.4 Ω, which rapidly decreases to 1.8 Ω within 10 min after the proton injection during the fuel cell process, then slowly decreases and stabilizes at 0.4 Ω at 60 min. It indicates it is 4 orders of magnitude easier to proceed, which suggests protons were produced from anode in a reaction called hydrogen oxidation reaction (HOR) ($H_2 \rightarrow 2H^+ + 2e^-$), then injected into the Eu_2O_3 moving to the cathode and joining the oxygen reduction process. On the other hand, after the introduction of hydrogen on one air side, the ORR caused by catalyzed ($O_2 \rightarrow O^{2-} + 2e^-$) no longer dominates,[49] and protons take over in ion transport therewith and make the ORR process transform into the proton fuel cell, i.e., $4H^+ + 4e^- + O_2 \rightarrow 2H_2O$,[49] though the original ORR still exists with less impact. Figure 3D depicts an example of such a fitting paired with a precise fragmentation of the impedance
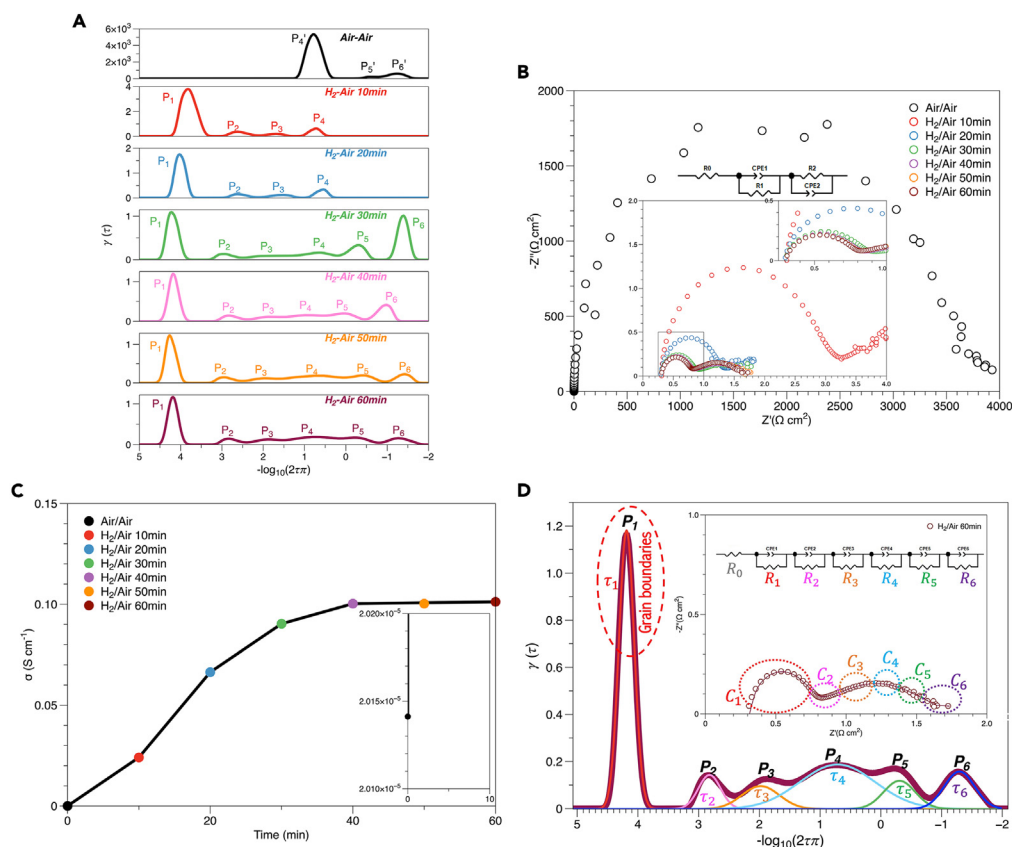
Figure 3. Results of the distribution of relaxation times analysis

(A) The DRT results of the cell at 520°C show several sub-processes which dynamically demonstrate the electrochemical proton injection and grain boundary conduction from air/air to H_2/air atmosphere.

(B and C) The calculated conductivities (C) are obtained from the EIS data (B) from air/air to H_2/air atmosphere. The cell resistance reduced dramatically over time and the related conductivity boost from 2.01×10^{-5} S/cm to 0.10 S/cm in an hour.

(D) The DRT plot corresponds to the sixtieth minute of hydrogen introduction is well-fitted with six peaks with its multi-segment circuit model. The peak P_1 corresponds to a C_1 value of 8.4×10^{-6} F, which is ascribed to the first semicircle grain-boundary arc of the proton-conducting Eu_2O_3, and its relaxation time (τ_1) is 1×10^{-5} s.

spectra with DRT data, whose conductivity is relatively stable, and hydrogen has been applied for 1 h to fit the characteristic capacitance investigation (Figure S7).

Therefore, this fuel cell device and its specific measurement conditions in the investigation differ significantly from a conventional fuel cell study; a small flow of H_2 is applied to control the anodic activation and enable the desired HOR happens, facilitating the transition from intrinsic possible electronic conduction to proton dominance and permitting the observation of the controlled conducting process at the required high proton conduction level by DRT analysis. By employing this unique methodology, the study gains insights into the electrochemical proton injection leading to surficial proton conduction phenomena and elucidate the mechanisms underlying the enhanced conductivity observed in the Eu_2O_3 material.

Further experiment was carried out to determine the proton conductivity dependence on hydrogen concentrations adjusted by mixing nitrogen; when the flow rate of hydrogen increases, the nitrogen is reduced by equal proportions so that the hydrogen concentration in the mixture starts from 0% to 100%. A proton injected into an oxide may be regarded simply as an interstitial proton, with $Kröger - Vink$ notation $H_i^{\cdot}$.[50] With hydrogen gas as the source, the injection of protons in oxides may be written as:

$$\frac{1}{2}H_2(g) = H_i^{\cdot} + e^{'}, K_1 = [H_i^{\cdot}]nP_{H_2}^{-1/2}$$ (Equation 3)

Where n denotes the conduction band (defect) electrons concentration and P denotes partial pressure. When protons are minority defects, all native defects, including defect electrons, are independent of P_{H_2} (at constant P_{O_2}). Hydrogen concentration $[H_i^{\cdot}]$ is then proportional to $P_{H_2}^{1/2}$. And since protons are movable exogenous ions, the conductivity of protons is proportional to the concentration of movable protons according to the Arrhenius relationship; the ionic conductivity is increased with increasing hydrogen concentration as shown in Figure 4.
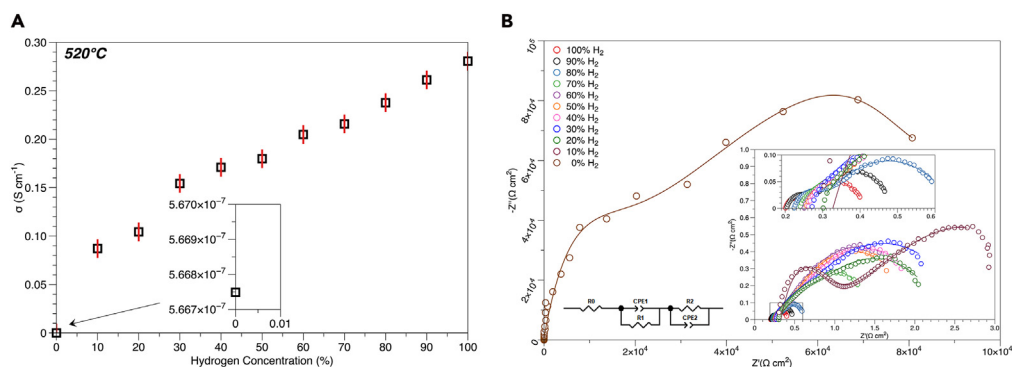
Figure 4. Results for the hydrogen mixed with nitrogen concentration cell experiment carried out on Eu_2O_3

(A and B) The calculated conductivities (A) are obtained from the EIS data (B) from N_2/N_2 to H_2/N_2 atmosphere at 520°C. The conductivity increases significantly from 5.6675×10^{-7} S/cm to 0.28055 S/cm, but still is proportional to the concentration of hydrogen changes.

Generally, protons can predominantly travel in two ways in oxides.[50] In the "free migration" mechanism, the proton moves by hopping between oxygen ions that are immobile as hosts. In the "vehicle mechanism," the proton rides as a passenger on a bigger ion, such as OH^- or H_3O^+. Based on the aforementioned experimental results as shown in Figure 4, free proton migration appears to dominate proton transport in oxides at high temperatures.[50] In Eu_2O_3, oxygen vacancies are introduced by the presence of varying valences:

$$Eu_2O_3 \rightarrow 2Eu'_{Eu} + V_o^{\cdot\cdot} + 3O_O^x \qquad \text{(Equation 4)}$$

The process of its reduction in the *Kröger − Vink* notation might be written as:

$$2Eu_{Eu}^x + O_O^x \rightarrow 2Eu'_{Eu} + V_o^{\cdot\cdot} + \frac{1}{2}O_2 \qquad \text{(Equation 5)}$$

Where Eu^{3+} at the lattice is placed by Eu^{2+} accompanying oxygen vacancy formation.

Eu_2O_3 can acquire protons ($OH_o^{\cdot}$) in the presence of hydrogen via a redox reaction known as protonation or hydrogenation, which is irrelevant to oxygen vacancies ($V_o^{\cdot\cdot}$) and proton defects can be produced.

$$H_2 + 2O_o^x \rightarrow 2OH_o^{\cdot} + 2e' \qquad \text{(Equation 6)}$$

During the fuel cell operation, protons can be injected and transported through the Eu_2O_3 electrolyte, where water is possible to formed at the cathode side; thus, further hydration reaction may also occur. At this point, oxygen vacancies can act as active or catalytic sites for hydrogen and water dissociation on surfaces, and then generate two proton defects in hydroxyl form $OH_o^{\cdot}$ as described in the following:

$$H_2O_{(g)} + O_o^x + V_o^{\cdot\cdot} \rightarrow 2OH_o^{\cdot} \qquad \text{(Equation 7)}$$

The surficial proton transport mechanism in $H-Eu_2O_3$ can be elucidated by taking into account the synergistic involvement of the proton-coupled electron transfer (PCET) via a cation redox couple mechanism in parallel with the oxygen vacancy mechanism.[51] The redox Eu^{3+} - Eu^{2+} couple signifies the transfer of electrons (e^-) between the Eu^{3+} and Eu^{2+} states on the surface of $H-Eu_2O_3$. This electron transfer is coupled with the proton transfer, thereby facilitating the surficial proton transport.[52] Meanwhile, the oxygen vacancies within $H-Eu_2O_3$ create localized electronic states to serve as diffusion pathways for H^+ ions, enabling the migration of protons and allowing for their movement across the material's surface. This oxygen vacancy mechanism contributes to the overall proton conductivity. Our aforementioned XPS analysis revealed the presence of the redox couple, providing evidence for the PCET process in addition to the oxygen vacancy mechanism. As shown in Figure S8, a transparent amorphous layer at the edge of the Eu_2O_3 sample can form more oxygen vacancies, defects and distortions due to irregular edge, enabling better construction of inter-lattice transport channels for protons. And a space charge zone/layer with a particle size of 0.245 nm was distributed on surface after the operation indicating that the Eu^{3+} on surface is reduced to divalent, resulting in more oxygen vacancies.

Therefore, surficial proton conduction of $H-Eu_2O_3$ involves a parallel process, and the conductivity can be boosted based on these mechanisms as discussed previously, which is illustrated in Figure 5. This comprehensive understanding provides a foundation for the design and development of high-performance proton conductors. By exploring the interplay between PCET and oxygen vacancy mechanisms, we can further optimize the proton conductivity of $H-Eu_2O_3$ and potentially apply this knowledge to the development of advanced proton-conducting materials for various energy-related applications.

Conclusions

This study presents a novel approach for developing influential proton conductors and provides valuable insights into the significance of surficial proton transport in enhancing proton conductivity in materials, particularly in wide bandgap semiconductor, Eu_2O_3. Through
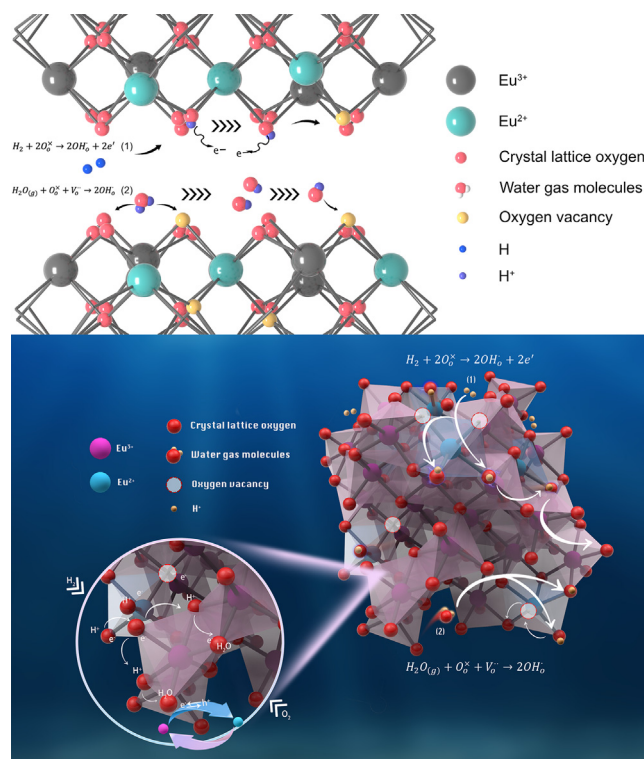
Figure 5. Schematic representation of proton conduction mechanisms for Eu₂O₃

The effect of hydrogen on it created protons that are adhered to the surface lattice of oxygen. When protons diffuse along the lattice oxygen of grain boundary, they migrate by continually breaking and forming bonds, causing the old hydroxyl group to dissipate and a new one to develop. The released electrons could increase the number of oxygen vacancies on the surface. Simultaneously, water molecules will interact with oxygen vacancies to produce hydroxyl groups, which will flow along the oxygen vacancies on the surface of the grain boundary. Base on that, the surficial proton transport mechanism can be completed by taking into account the synergistic involvement of the proton-coupled electron transfer (PCET) via a redox Eu^{3+} - Eu^{2+} couple mechanism in parallel with the oxygen vacancy mechanism.

a comprehensive analysis involving EIS, assembled cells, proton isotopic and filtering measurements, and DRT analysis of proton injection and conduction processes, we found that grain boundary i.e., surficial proton transport is the underlying mechanisms in Eu_2O_3. The interplay between PCET and oxygen vacancy mechanisms plays the important role, showcasing a promise for applying this knowledge to the development of advanced proton-conducting materials. We have successfully achieved a high proton conductivity of 0.16 S/cm, primarily driven by surface-led proton transport and demonstrated a peak power density of 660.9 mW/cm^2 at 520°C. These results, along with the developed methodologies and knowledge gained from this study provide new directions for the design and development of advanced SOFCs/PCFCs and beyond.

Limitations of the study

In this work, the cell was fabricated by laboratorial dry powder pressing and assembly of the cell, resulting in a delamination phenomenon in the SEM image. Stability testing was not involved in this study, which is beyond this work capacity on material fundamental and proton transport mechanism. At present, it is feasible to verify the PCET mechanism by DRT analysis, there is still a need for more detailed simulation soft program to deepen this valuable topic.

STAR★METHODS

Detailed methods are provided in the online version of this paper and include the following:

- KEY RESOURCES TABLE
- RESOURCE AVAILABILITY
  - Lead contact
  - Materials availability
  - Data and code availability
- EXPERIMENTAL MODEL AND STUDY PARTICIPANT DETAILS

SUPPLEMENTAL INFORMATION

ACKNOWLEDGMENTS

AUTHOR CONTRIBUTIONS

Conceptualization, S.W. and B.Z.; Methodology, S.W. and B.Z.; Investigation, S.W. and H.W.; Writing – Original Draft, S.W.; Writing Review & Editing, M.A.K.Y.S., P.D.L., and B.Z.; Funding Acquisition, B.Z.; Resources, B.Z.; Supervision, B.Z.

DECLARATION OF INTERESTS

The authors declare no competing financial interests.

INCLUSION AND DIVERSITY

We support inclusive, diverse, and equitable conduct of research.

REFERENCES

1. Iwahara, H., Uchida, H., Ono, K., and Ogaki, K. (1988). Proton conduction in sintered oxides based on BaCeO3. J. Electrochem. Soc. *135*, 529–533.

2. Katahira, K., Kohchi, Y., Shimura, T., and Iwahara, H. (2000). Protonic conduction in Zr-substituted BaCeO3. Solid State Ionics *138*, 91–98.

3. Hibino, T., Hashimoto, A., Suzuki, M., and Sano, M. (2002). A solid oxide fuel cell using Y-doped BaCeO3 with Pd-loaded FeO anode and Ba0. 5Pr0. 5CoO3 cathode at low temperatures. J. Electrochem. Soc. *149*, A1503.

4. Wachsman, E.D., and Lee, K.T. (2011). Lowering the temperature of solid oxide fuel cells. Science *334*, 935–939.

5. Chen, G., Zhu, B., Deng, H., Luo, Y., Sun, W., Liu, H., Zhang, W., Wang, X., Qian, Y., Hu, X., et al. (2018). Advanced fuel cell based on perovskite La–SrTiO3 semiconductor as the electrolyte with superoxide-ion conduction. ACS Appl. Mater. Interfaces *10*, 33179–33186.

6. Xing, Y., Wu, Y., Li, L., Shi, Q., Shi, J., Yun, S., Akbar, M., Wang, B., Kim, J.S., and Zhu, B. (2019). Proton shuttles in CeO2/CeO2− δ core–shell structure. ACS Energy Lett. *4*, 2601–2607.

7. Dong, W., Tong, Y., Zhu, B., Xiao, H., Wei, L., Huang, C., Wang, B., Wang, X., Kim, J.S., and Wang, H. (2019). Semiconductor TiO 2 thin film as an electrolyte for fuel cells. J. Mater. Chem. A Mater. *7*, 16728–16734.

8. Lu, Y., Zhu, B., Shi, J., and Yun, S. (2022). Advanced low-temperature solid oxide fuel cells based on a built-in electric field. Energy Mater. *1*, 100007.

9. Rauf, S., Zhu, B., Yousaf Shah, M.A.K., Tayyab, Z., Attique, S., Ali, N., Mushtaq, N., Wang, B., Yang, C., Asghar, M.I., and Lund, P.D. (2020). Application of a triple-conducting heterostructure electrolyte of Ba0. 5Sr0. 5Co0. 1Fe0. 7Zr0. 1Y0. 1O3− δ and Ca0. 04Ce0. 80Sm0. 16O2− δ in a high-performance low-temperature solid oxide fuel cell. ACS Appl. Mater. Interfaces *12*, 35071–35080.

10. Shah, M.Y., Lu, Y., Mushtaq, N., Singh, M., Rauf, S., Yousaf, M., and Zhu, B. (2022). ZnO/MgZnO heterostructure membrane with type II band alignment for ceramic fuel cells. Energy Mater. *2*, 200031.

11. Wei, W., Xu, T., Zhang, Y., Huang, Y., Wang, X., and Yan, S. (2022). Designing Composite BaCe0. 4Zr0. 4Y0. 1Yb0. 1O3-δ-Sm0. 2Ce0. 8O2-δ Heterostructure Electrolyte for Low-Temperature Ceramic Fuel Cell (LT-CFCs). Crystals *13*, 41.

12. Kumar, S., Prakash, R., Choudhary, R.J., and Phase, D.M. (2015). Structural, XPS and magnetic studies of pulsed laser deposited Fe doped Eu2O3 thin film. Mater. Res. Bull. *70*, 392–396.

13. Chen, W., Joly, A.G., Kowalchuk, C.M., Malm, J.O., Huang, Y., and Bovin, J.O. (2002). Structure, luminescence, and dynamics of Eu2O3 nanoparticles in MCM-41. J. Phys. Chem. B *106*, 7034–7041.

14. Chaudhary, S., and Umar, A. (2016). Glycols functionalized fluorescent Eu2O3 nanoparticles: Functionalization effect on the structural and optical properties. J. Alloys Compd. *682*, 160–169.

15. Makhluf, S.B.D., Arnon, R., Patra, C.R., Mukhopadhyay, D., Gedanken, A., Mukherjee, P., and Breitbart, H. (2008). Labeling of sperm cells via the spontaneous penetration of Eu3+ ions as nanoparticles complexed with PVA or PVP. J. Phys. Chem. C *112*, 12801–12807.

16. Zhou, J., He, J., Wang, T., Chen, X., and Sun, D. (2009). Synergistic effect of RE2O3 (RE= Sm, Eu and Gd) on Pt/mesoporous carbon catalyst for methanol electro-oxidation. Electrochim. Acta *54*, 3103–3108.

17. Mohamed, W.S., and Abu-Dief, A.M. (2018). Synthesis, characterization and photocatalysis enhancement of Eu2O3-ZnO mixed oxide nanoparticles. J. Phys. Chem. Solid. *116*, 375–385.

18. Wang, F., Hu, E., Wu, H., Yousaf, M., Jiang, Z., Fang, L., Wang, J., Kim, J.S., and Zhu, B. (2022). Surface-Engineered Homostructure for Enhancing Proton Transport. Small Methods *6*, 2100901.

19. Wang, F., Hu, E., Wang, J., Yu, L., Hong, S., Kim, J.S., and Zhu, B. (2022). Tuning La 2 O 3 to high ionic conductivity by Ni-doping. Chem. Commun. *58*, 4360–4363.

20. Chen, Q.H., Shi, S.Y., and Zhang, W.G. (2009). Study on the structure and luminescent properties of the coordinated Eu2O3 ethanol colloids. Mater. Chem. Phys. *114*, 58–62.

21. Kang, J.G., Jung, Y., Min, B.K., and Sohn, Y. (2014). Full characterization of Eu (OH) 3 and Eu2O3 nanorods. Appl. Surf. Sci. *314*, 158–165.

22. Zha, C., Sun, X., Li, N., and Yu, S. (2014). In-situ synthesis of hydrotalcite and its application in separation of simulated radionuclide Eu (III). Korean J. Chem. Eng. *31*, 1859–1864.

23. Sun, H., Hu, K., Lou, H., and Zheng, X. (2008). Biodiesel Production from Transesterification of Rapeseed Oil Using KF/Eu 2O 3 as a Catalyst. Energy Fuels *22*, 2756–2760.

24. Ahlawat, R., Rani, N., and Goswami, B. (2018). Synthesis and characterizations of Eu2O3 nanocrystallites and its effect on optical investigations of Eu3+, Eu2+: SiO2 nanopowder. J. Alloys Compd. *743*, 126–135.

25. Pathan, A.A., Desai, K.R., and Bhasin, C.P. (2017). Synthesis of La2O3 nanoparticles using glutaric acid and propylene glycol for future CMOS applications. Int. J. Nano. Chem. *3*, 21–25.

26. Mu, Q., and Wang, Y. (2011). Synthesis, characterization, shape-preserved transformation, and optical properties of La (OH) 3, La2O2CO3, and La2O3 nanorods. J. Alloys Compd. *509*, 396–401.

27. Wong, K.L., Law, G.L., Murphy, M.B., Tanner, P.A., Wong, W.T., Lam, P.K.S., and Lam, M.H.W. (2008). Functionalized europium nanorods for *in vitro* imaging. Inorg. Chem. *47*, 5190–5196.

28. Kreuer, K.D. (1997). On the development of proton conducting materials for technological applications. Solid State Ionics *97*, 1–15.

29. Mehta, M., Kodan, N., Kumar, S., Kaushal, A., Mayrhofer, L., Walter, M., Moseler, M., Dey, A., Krishnamurthy, S., Basu, S., and Singh, A.P. (2016). Hydrogen treated anatase TiO 2: a new experimental approach and further insights from theory. J. Mater. Chem. A Mater. *4*, 2670–2681.

30. Greczynski, G., and Hultman, L. (2018). Reliable determination of chemical state in x-ray photoelectron spectroscopy based on sample-work-function referencing to adventitious carbon: resolving the myth of apparent constant binding energy of the C 1s peak. Appl. Surf. Sci. *451*, 99–103.

31. Peng, L., Yu, Z., Zhang, M., Zhen, S., Shen, J., Chang, Y., Wang, Y., Li, A., Deng, Y., and Li, A. (2021). A novel battery separator coated by a europium oxide/carbon nanocomposite enhances the performance of lithium sulfur batteries. Nanoscale *13*, 16696–16704.

32. Cho, E.J., and Oh, S.J. (1999). Surface valence transition in trivalent Eu insulating compounds observed by photoelectron spectroscopy. Phys. Rev. B *59*, R15613–R15616.

33. Dupin, J.C., Gonbeau, D., Vinatier, P., and Levasseur, A. (2000). Systematic XPS studies of metal oxides, hydroxides and peroxides. Phys. Chem. Chem. Phys. *2*, 1319–1324.

34. Wang, B., Wang, Y., Fan, L., Cai, Y., Xia, C., Liu, Y., Raza, R., van Aken, P.A., Wang, H., and Zhu, B. (2016). Preparation and characterization of Sm and Ca co-doped ceria–La 0.6 Sr 0.4 Co 0.2 Fe 0.8 O 3— δ semiconductor–ionic composites for electrolyte-layer-free fuel cells. J. Mater. Chem. A Mater. *4*, 15426–15436.

35. Cai, Y., Wang, B., Wang, Y., Xia, C., Qiao, J., van Aken, P.A., Zhu, B., and Lund, P. (2018). Validating the technological feasibility of yttria-stabilized zirconia-based semiconducting-ionic composite in intermediate-temperature solid oxide fuel cells. J. Power Sources *384*, 318–327.

36. Chan, S.H., Khor, K.A., and Xia, Z.T. (2001). A complete polarization model of a solid oxide fuel cell and its sensitivity to the change of cell component thickness. J. Power Sources *93*, 130–140.

37. Qiao, Z., Xia, C., Cai, Y., Afzal, M., Wang, H., Qiao, J., and Zhu, B. (2018). Electrochemical and electrical properties of doped CeO2-ZnO composite for low-temperature solid oxide fuel cell applications. J. Power Sources *392*, 33–40.

38. Chen, G., Liu, H., He, Y., Zhang, L., Asghar, M.I., Geng, S., and Lund, P.D. (2019). Electrochemical mechanisms of an advanced low-temperature fuel cell with a SrTiO 3 electrolyte. J. Mater. Chem. A Mater. *7*, 9638–9645.

39. Hayd, J., and Ivers-Tiffée, E. (2013). Detailed electrochemical study on nanoscaled La0. 6Sr0. 4CoO3-δ SOFC thin-film cathodes in dry, humid and CO2-containing atmospheres. J. Electrochem. Soc. *160*, F1197–F1206.

40. Zhang, Y., Chen, Y., Li, M., Yan, M., Ni, M., and Xia, C. (2016). A high-precision approach to reconstruct distribution of relaxation times from electrochemical impedance spectroscopy. J. Power Sources *308*, 1–6.

41. Zhang, Y., Chen, Y., Yan, M., and Chen, F. (2015). Reconstruction of relaxation time distribution from linear electrochemical impedance spectroscopy. J. Power Sources *283*, 464–477.

42. Sumi, H., Yamaguchi, T., Hamamoto, K., Suzuki, T., and Fujishiro, Y. (2013). High performance of La0. 6Sr0. 4Co0. 2Fe0. 8O3–Ce0. 9Gd0. 1O1. 95 nanoparticulate cathode for intermediate temperature microtubular solid oxide fuel cells. J. Power Sources *226*, 354–358.

43. Wang, X., Ma, Z., Zhang, T., Kang, J., Ou, X., Feng, P., Wang, S., Zhou, F., and Ling, Y. (2018). Charge-transfer modeling and polarization DRT analysis of proton ceramics fuel cells based on mixed conductive electrolyte with the modified anode–electrolyte interface. ACS Appl. Mater. Interfaces *10*, 35047–35059.

44. Li, M., Sun, Z., Yang, W., Hong, T., Zhu, Z., Zhang, Y., Wu, X., and Xia, C. (2016). Mechanism for the enhanced oxygen reduction reaction of La 0.6 Sr 0.4 Co 0.2 Fe 0.8 O 3— δ by strontium carbonate. Phys. Chem. Chem. Phys. *19*, 503–509.

45. Wang, J., Li, Z., Zang, H., Sun, Y., Zhao, Y., Wang, Z., Zhu, Z., Wei, Z., and Zheng, Q. (2022). BaZr0. 1Fe0. 9-xNixO3-δ cubic perovskite oxides for protonic ceramic fuel cell cathodes. Int. J. Hydrogen Energy *47*, 9395–9407.

46. Yu, S., Wang, Z., Yang, L., Liu, J., Guan, R., Xiao, Y., and He, T. (2021). Enhancing the sinterability and electrical properties of BaZr0. 1Ce0. 7Y0. 2O3-δ proton-conducting ceramic electrolyte. J. Am. Ceram. Soc. *104*, 329–342.

47. Guo, R., Li, D., Guan, R., Kong, D., Cui, Z., Zhou, Z., and He, T. (2022). Sn–Dy–Cu Triply Doped BaZr0. 1Ce0. 7Y0. 2O3− δ: a chemically stable and highly proton-conductive electrolyte for low-temperature solid oxide fuel cells. ACS Sustain. Chem. Eng. *10*, 5352–5362.

48. Guo, R., and He, T. (2022). High-entropy perovskite electrolyte for protonic ceramic fuel cells operating below 600 C. ACS Mater. Lett. *4*, 1646–1652.

49. Bin, Z., Youquan, M., Chen, X., Baoyuan, W., Jung-Sik, K., Peter, L., and Tao, L. (2021). Nano-scale view into solid oxide fuel cell and semiconductor membrane fuel cell: material and technology. Energy Mater. *1*, 2.

50. Norbya, T. (1990). Proton conduction in oxides. Solid State Ionics *40–41*, 857–862.

51. Wu, Y., Xia, C., Zhang, W., Yang, X., Bao, Z.Y., Li, J.J., and Zhu, B. (2016). Natural hematite for next-generation solid oxide fuel cells. Adv. Funct. Mater. *26*, 938–942.

52. Tyburski, R., Liu, T., Glover, S.D., and Hammarström, L. (2021). Proton-coupled electron transfer guidelines, fair and square. J. Am. Chem. Soc. *143*, 560–576.

STAR★METHODS

KEY RESOURCES TABLE

REAGENT or RESOURCE	SOURCE	IDENTIFIER
Chemicals, peptides, and recombinant proteins		
Eu_2O_3 (99.9%)	Shanghai Macklin Biochemical Technology Co., Ltd	CAS: 1308-96-9
Software and algorithms		
DataGraph	Visual Data Tools	http://www.visualdatatools.com/DataGraph
Origin 2018	OriginLab	https://www.originlab.com
MATLAB R2022b	MathWorks	https://www.mathworks.com
Other		
Electrochemical workstation, Energy Lab XM	AMETEK Company	https://www.ametek.com
Electrochemical workstation, CHI660E	CH Instruments Company	http://www.chinstr.com
Scanning electron microscope	Hitachi Company	https://www.hitachi-hightech.com
X-ray diffractometer, Model ULTIMA IV	Rigaku Company	www.rigaku.com
Transmission electron microscopy, Talos F200S G2	FEI Company	www.fei.com
X-ray photoelectron spectroscopy, Escalab Xi+	FEI Company	www.fei.com
Fourier transform infrared spectroscopy	PerkinElmer Company	www.perkinelmer.com
Electron paramagnetic resonance EMX-PLUS spectrometer	Bruker Company	www.bruker.com

RESOURCE AVAILABILITY

Lead contact

Further information and requests for resources should be directed to and will be fulfilled by the Lead Contact, Bin Zhu (zhu-bin@seu.edu.cn).

Materials availability

This study did not generate new unique reagents.

Data and code availability

- All data reported in this paper will be shared by the lead contact upon request.
- This paper does not report original code.
- Any additional information required to reanalyze the data reported in this paper is available from the lead contact upon request.

EXPERIMENTAL MODEL AND STUDY PARTICIPANT DETAILS

Chemicals and materials

A commercial Eu_2O_3 (99.9%, Macklin, China) chemical was purchased for use. The commercially available $LiNi_{0.8}Co_{0.15}Al_{0.05}O_2$ -oxide (NCAL) powder was used as an electrode material obtained from Tianjin Xinli Science &Technology Joint Stock Ltd., China.

The proton filter layer (O^{2-}/e^- blocking layer) $BaZr_{0.3}Ce_{0.6}Y_{0.1}O_{3-\delta}$ (BZCY) was synthesized by a gel-combustion method. $Ba(NO_3)_2$, $Zr(NO_3)_4$, $Ce(NO_3)_2 \cdot 6H_2O$, and $Y(NO_3)_3 \cdot 6H_2O$ were weighted in a desired mole ratio and dissolved in ethylene diamine tetra acetic acid (EDTA) under continuous stirrings to prepare BZCY sample solution. Later, $C_6H_8O_7 \cdot H_2O$ and $C_{10}H_{16}N_2O_8$ were added to the solution with the mole ratio of cation: citric acid: EDTA = 1: 1.5: 1. Then $NH_3 \cdot H_2O$ was used to adjust the solution pH to approximately 9 when the solution became transparent. The solution was stirred at 90°C for 4 h to evaporate the water, and a grey gel was attained. Finally, the gel was dried in an oven at 120°C for 6 hours, then grounded and calcined at 1000°C in the air for 5 h, and the obtained powder was adequately ground to get the final BZCY.

Electrode preparation

The fuel cell device for electrochemically injecting protons and performance studies was fabricated using the Eu_2O_3 powder as electrolyte and NCAL as electrodes. Pipetting ethanol and terpineol into NCAL powder at a volume ratio of 1:1 yielded a slurry that was then used to cover one side of the nickel foam. The electrodes were obtained by drying the nickel foam pasted NCAL in an oven at 120°C for 45 minutes. The Eu_2O_3 powder was pressed for 60 seconds at 6 MPa to form an electrolyte sheet with a diameter of 13 mm and an electrolyte layer thickness of 0.72 mm. Then the electrodes and electrolytes were assembled sequentially to get the final symmetrical fuel cell. The resultant cell was 4.43 mm thick with an active working area of 0.64 cm^2.

METHOD DETAILS

Electrochemistry test

The fuel cell operation itself is an in-situ proton injection process, or protonation was conducted on a fuel cell device fabricated using the Eu_2O_3 as the electrolyte because the pristine Eu_2O_3 has not any proton contained. Before the operation, the fuel cell device was preheated for an hour at 500°C in a tubular furnace. Then we will adjust the temperature to 520°C by supplying H_2 at anode and air at cathode through steel tubes to activate the fuel cell and start measurements. The fuel cell performance was measured every 20°C from 520°C to 400°C on a digital instrument (ITECH8511), and the voltage and current (density) were collected. Each measuring point was tested after waiting for the voltage to fully stabilize.

The electrochemical impedance spectra (EIS) were measured under fuel cell open circuit voltage (OCV) conditions by a potentiostat (CHI660E) at a frequency range of 10^{-1}–10^5 Hz in H_2/air atmosphere at 400-520°C and by Energy Lab XM (AMETEK) at a frequency range of 10^{-2}–10^6 Hz in air/air and H_2/air atmosphere at 520°C. And the acquired impedance data were fitted via the Z-view and distribution of relaxation time (DRT). The conductivity was determined by simulating the resistance using EIS data. Impedance spectroscopy is performed first, followed by cell performance testing.

Characterization

X-ray diffraction (XRD) was utilized to determine the crystalline phases of the Eu_2O_3 sample. Its pattern was recorded in the 2θ range of 5-85° using an automated X-ray diffractometer (Model ULTIMA IV, Rigaku, Japan) with Cu Kα radiation (λ=1.5418Å) at a scan rate of 2°/min. Scanning electron microscopy (SEM; Hitachi Company, Japan) and high-resolution transmission electron microscopy (HR-TEM; Talos F200S G2, FEI Company, USA) were employed to investigate the morphological microstructure features and the cell's cross-section. The Escalab Xi+ (Thermo Fisher, USA) was utilized for X-ray photoelectron spectroscopy (XPS) investigation with Al-Ka radiation. The electron paramagnetic resonance (EPR) spectra were recorded on a Bruker EMX-PLUS spectrometer with a center magnetic field of 6900 G and a frequency of 9.74 GHz. The Fourier transform infrared (FTIR) spectroscopy was conducted on a PerkinElmer Frontier in the range of 4000-600cm^{-1}.

Calculation method of the Distribution of Relaxation Time (DRT)

Electrochemical impedance spectroscopy (EIS) analysis using the distribution of relaxation time (DRT) method can identify the polarization processes with a high resolution; consequently, the polarization processes overlapping in the EIS curve can be clearly distinguished in the DRT curve. The DRT method is calculated by DRT tools which is MATLAB GUI that allows users to analyze EIS data. The computation of the DRT is based on Tikhonov regularization with continuous function discretization.

The DRT function F(τ) can be described as

$$F(\tau) = \tau G(\tau)\ln(10) = \frac{-\ln(10)}{\pi}\left[Z''\left(e^{-\ln\tau+j\pi/2}\right) + Z''\left(e^{-\ln\tau-j\pi/2}\right)\right] \qquad \text{(Equation 8)}$$

where Z″ refers to the imaginary part of Z; τ is the relaxation time related to the frequency f according to τ = 1/2πf; and F(τ) conforms to the equation

$$\int_{-\infty}^{\infty} F(\tau)d\log_{10}\tau = Z'(0) - Z'(\infty) \qquad \text{(Equation 9)}$$

where $Z'(0) - Z'(\infty)$ equals the whole polarization resistance. F(τ) can be calculated using the quadratic programming based on the EIS measurements data.

The DRT method allows the dominant reflexes and their corresponding resistances to be revealed as bounded by the log f axis and the distribution function. After getting the peak segmentation results, the relaxation time and resistance data are obtained. Since each chemical process overlapping in the EIS curve has its own unique data characteristics (resistance, capacitance, relaxation time, and frequency range), the chemical process corresponding to each peak can be identified by comparing the actual results with calculation results.